FDTD Time Domain Near- to Far-Zone Transformation Above a Lossy Dielectric Half-space

Torleif Martin, Lars Pettersson
FOA Defence Research Establishment
Dept. of Microwave Technology
P.O. Box 1165
S-581 11 Linköping, SWEDEN

Abstract: *Near- to Far-zone transformation in the Finite-Difference Time-Domain (FDTD) method can be performed in either the time domain or in the frequency domain. For free space conditions, the time domain near- to far-zone transformation is generally much faster and more memory efficient to use, when we require results at a large number of frequency points at a small number of far-zone directions. However when a lossy dielectric half-space is present, representing the ground, the frequency domain transformation has been favored since the Green's functions involved are relatively simple to express in the frequency domain compared with the efforts needed to transform these expressions into the time domain. This paper describes a combined time- and frequency domain near- to far-zone transformation above a lossy dielectric half-space, where it is not necessary to transform the equivalent currents into the frequency domain. This transformation is much faster than the pure frequency domain transformation and comparisons are made between the two different approaches. For validation purposes, scattering of a dihedral above a lossy dielectric half-space is considered.*

1 Introduction

The FDTD method is very useful for broadband scattering applications involving complex object geometries and material parameters. One area of interest has been ground penetrating radar and synthetic aperture radar simulations in geoscience applications and ground target detection, where the ground must be included in the simulations. Lately, a number of papers have been published in this area [1-6] where either FDTD or the Method of Moment has been used. Both methods have their advantages and disadvantages depending on the problem type. Time-domain methods such as FDTD have the advantage of generating results for the entire frequency range in a single simulation.

A near- to far-zone transformation is necessary in FDTD since only the near fields are accessible in the computational volume. When performing the near- to far-zone transformation in the frequency domain, the equivalent surface currents on a closed surface are transformed into the frequency domain by a Discrete Fourier Transform (DFT). The far-zone vector potentials can then be easily calculated by multiplying the equivalent currents with the Green's function and summing the contributions over the closed surface.

Alternatively, the near- to far-zone transformation can be performed in the time-domain. For free-space conditions, the Green's function corresponds to a time shift of the equivalent currents. Using this type of transformation the fields, at retarded times for each position of the surface currents on the closed surface, must be accumulated and stored in "far-zone arrays", one for each far-zone direction [7],[8].

Depending on the problem type either approach has its advantages. If a large number of far-zone angles are to be considered, at a small number of frequencies, the frequency domain transformation is probably preferable. On the other hand, if only a few far-zone angles are desired over a large number of frequencies, the time-domain transformation is generally faster to use.

When the scattering object is placed on or below the ground the transformation procedure becomes more complicated. The free-space Green's function must be replaced by a Green's function that takes reflection and refraction into account. If only the far-zone field is considered, this Green's function can be expressed as a function of the Fresnel reflection and refraction coefficients, e.g. [9]. If losses are present in the ground material, the Green's functions include a frequency dependency which makes it simpler to perform the near- to far-zone transformation in the frequency domain, rather than to use a time consuming convolution between the fields and a complicated time-domain Green's function. Therefore it is generally favorable to perform the near- to far-zone transformation in the frequency domain, after transforming the equivalent surface currents into the frequency do-

main by a DFT.

However, for applications with few scattering angles, significant time savings can be achieved by combining the time-domain and frequency domain algorithms. The far-zone contribution of the equivalent currents can be sorted into different time-domain arrays, each corresponding to surface integrals of the vector potentials in the time-domain. After the FDTD execution, these vector potentials can then be transformed into the frequency domain and multiplied with different frequency dependent parts of the Green's function.

This paper describes the transformation method and gives examples of time savings that can be achieved. A dihedral placed above lossy ground is used as an test object and results using both frequency-domain and time-domain transformations in FDTD are presented. For validation purposes, comparisons are also made with the method of moment technique which includes the Sommerfeld type of Green's function (NEC-3).

2 Theory

By reciprocity, near- to far-zone transformations can be applied in the same way as calculating incident plane wave fields at the source points. For scattering problems including the ground, this type of transformation applied in the frequency domain was described in [1]. In [3] results using a similar near- to far-zone transformation were presented, where calculations of the equivalent surface currents were performed according to [10]. In [3] it was also shown that these surface currents are consistent with the FDTD-version of the reciprocity theorem. The main feature of these surface currents is that they are calculated at two different surfaces; one for the E-fields and one for the H-fields, separated with a half cell.

Using the reciprocity theorem, the far-zone Green functions can be easily expressed in terms of Fresnel reflection and refraction coefficients. The general expression for the far-field parallel to a unit vector $\hat{\mathbf{p}}$ can be written as [3]

$$\begin{aligned}\mathbf{E}_s(\mathbf{r})\cdot\hat{\mathbf{p}} &= -i\omega\mu_0 \iint_S \left[(\hat{\mathbf{n}}\times\mathbf{H}_s)\cdot\overline{\overline{\mathbf{G}}}_e\cdot\hat{\mathbf{p}}\right] dS' \\ &+ \iint_S \left[(\hat{\mathbf{n}}\times\mathbf{E}_s)\cdot\overline{\overline{\mathbf{G}}}_m\cdot\hat{\mathbf{p}}\right] dS'. \qquad (1)\end{aligned}$$

where we have adopted the notation of dyadic Green functions described in [11]. $\overline{\overline{\mathbf{G}}}_e$ and $\overline{\overline{\mathbf{G}}}_m$ are the electric and magnetic (dyadic) far-zone Green's functions for a homogeneous lossy dielectric half-space.

Let an infinitesimal test current source be placed in the far-zone (with respect to the integration surface S in (1)). Using a normalization factor as in [11], this test current source can be written as

$$\mathbf{J}_t = -\frac{\hat{\mathbf{p}}}{i\omega\mu_0}\delta^3(\mathbf{r}'-\mathbf{r}). \qquad (2)$$

Then we can recognize the reciprocity theorem if we identify

$$\mathbf{E}_t = \overline{\overline{\mathbf{G}}}_e\cdot\hat{\mathbf{p}} \qquad (3)$$

as the electric field from the small current source (2) in the far-zone. The corresponding magnetic field $\mathbf{H}_t$ is related to $\overline{\overline{\mathbf{G}}}_m$ through

$$-i\omega\mu_0\mathbf{H}_t = \overline{\overline{\mathbf{G}}}_m\cdot\hat{\mathbf{p}} \qquad (4)$$

since

$$\nabla\times\overline{\overline{\mathbf{G}}}_e = \overline{\overline{\mathbf{G}}}_m. \qquad (5)$$

The desired electric field in the far-zone is calculated at the test current source position above the surface by (1). When the distance r goes to infinity the incident field from the test current source can be approximated by a plane wave, and the electric dyadic Green function can be expressed in terms of Fresnel reflection and refraction coefficients. Note that it is assumed that $\hat{\mathbf{p}}\perp\hat{\mathbf{r}}$ in the derivations below. As an example, the far-zone Green's function projected on $\hat{\mathbf{p}}$, for source vectors $\mathbf{r}'$ above the surface (indicated with superscript a), becomes

$$\overline{\overline{\mathbf{G}}}_e^a(\mathbf{r},\mathbf{r}')\cdot\hat{\mathbf{p}} = \frac{e^{-ikr}}{4\pi r}\left(\bar{\bar{\mathbf{I}}}e^{ik\hat{\mathbf{r}}\cdot\mathbf{r}'} + \overline{\overline{\mathbf{R}}}_e e^{ik\hat{\mathbf{r}}\cdot\mathbf{r}_r'}\right)\cdot\hat{\mathbf{p}} \qquad (6)$$

where $\bar{\bar{\mathbf{I}}}$ is the identity matrix, $\overline{\overline{\mathbf{R}}}_e$ is a matrix containing the reflection coefficients, see (8) below, and $\mathbf{r}_r'$ is the mirrored position vector with respect to the ground level. The position vectors $\mathbf{r}'$ and $\mathbf{r}_r'$ are shown in Fig 1. They are defined relative to a phase center, preferable in the middle of the computational volume. If we choose the plane of incidence to be a X-Z -plane and if we divide the vector $\hat{\mathbf{p}}$ into components parallel and perpendicular to this plane,

$$\hat{\mathbf{p}} = p_{\parallel}\cos\theta\hat{\mathbf{x}} + p_{\perp}\hat{\mathbf{y}} - p_{\parallel}\sin\theta\hat{\mathbf{z}}. \qquad (7)$$

In this case the dyadic $\overline{\overline{\mathbf{R}}}_e$ becomes

$$\overline{\overline{\mathbf{R}}}_e = \begin{pmatrix} -\Gamma_{\parallel} & 0 & 0 \\ 0 & \Gamma_{\perp} & 0 \\ 0 & 0 & \Gamma_{\parallel} \end{pmatrix} \qquad (8)$$

where the reflection coefficients are, according to [9], using a slightly different notation,

$$\Gamma_{\parallel} = \frac{n^2\cos\theta - \sqrt{n^2-\sin^2\theta}}{n^2\cos\theta + \sqrt{n^2-\sin^2\theta}} \qquad (9)$$

$$\Gamma_{\perp} = \frac{\cos\theta - \sqrt{n^2-\sin^2\theta}}{\cos\theta + \sqrt{n^2-\sin^2\theta}} \qquad (10)$$

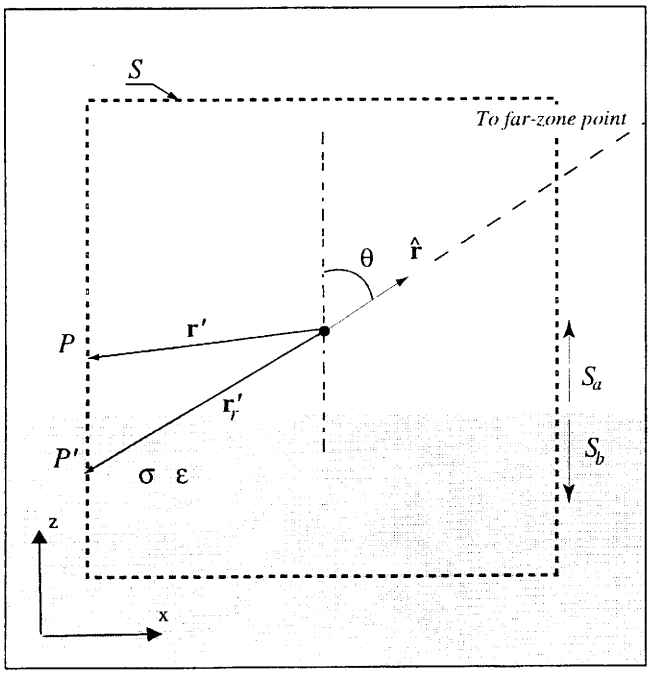

Figure 1: *Slice of the computational volume. Vectors used in the derivation of the Green's function from sources on S_a above the surface are shown.*

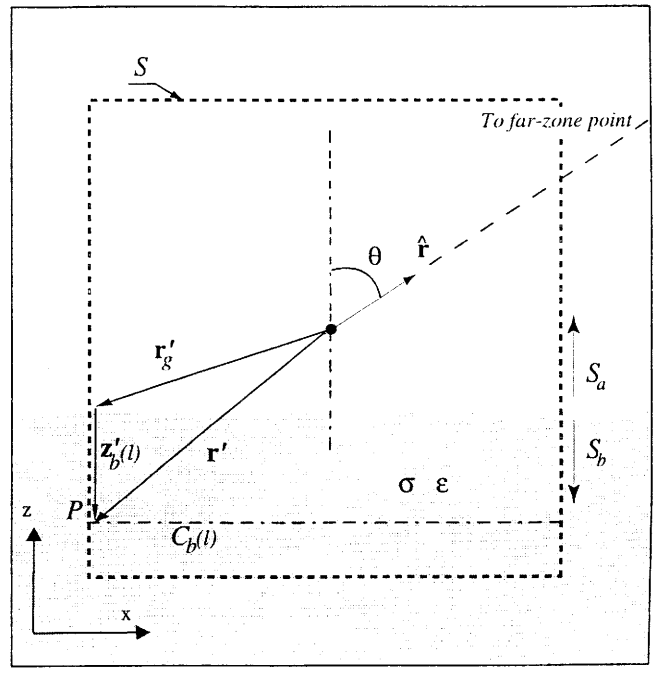

Figure 2: *Slice of the computational volume. Vectors used in the derivation of the Green's function from sources on S_b below the surface are shown.*

where we assume a non-magnetic ground. The index of refraction, n for the lower half-space is

$$n = \sqrt{\varepsilon_r + \frac{\sigma}{i\omega\varepsilon_0}}. \tag{11}$$

The corresponding Green's function projected on $\hat{\mathbf{p}}$, for a source below the surface (indicated with superscript b) can be written as

$$\overline{\overline{\mathbf{G}}}_e^{\,b} \cdot \hat{\mathbf{p}} = \frac{e^{-ikr}}{4\pi r} \overline{\overline{\mathbf{T}}}_e e^{ik\hat{\mathbf{r}}\cdot\mathbf{r}_g{}'} e^{ikz_b{}'\sqrt{n^2-\sin^2\theta}} \cdot \hat{\mathbf{p}} \tag{12}$$

where k is the free space wave number. The vectors $\mathbf{r}_g{}'$ and $\mathbf{z}_b{}' = z_b{}'\hat{\mathbf{z}}$ are components of the $\mathbf{r}'$ vector pointing to a source point P on S_b below the ground, via the projection on the ground level, see Fig. 2 ($z_b{}' < 0$ in (12)).

The transmission matrix $\overline{\overline{\mathbf{T}}}_e$ becomes

$$\overline{\overline{\mathbf{T}}}_e = \begin{pmatrix} 1-\Gamma_{\parallel} & 0 & 0 \\ 0 & 1+\Gamma_{\perp} & 0 \\ 0 & 0 & \frac{1}{n^2}(1+\Gamma_{\parallel}) \end{pmatrix}. \tag{13}$$

The corresponding magnetic Green's functions projected on $\hat{\mathbf{p}}$ can be derived as

$$\overline{\overline{\mathbf{G}}}_m^{\,a} \cdot \hat{\mathbf{p}} = i\frac{e^{-ikr}}{4\pi r}\left(\mathbf{k} \times \overline{\overline{\mathbf{I}}} e^{ik\hat{\mathbf{r}}\cdot\mathbf{r}'} + \mathbf{k}_r \times \overline{\overline{\mathbf{R}}}_e e^{ik\hat{\mathbf{r}}\cdot\mathbf{r}_r{}'}\right) \cdot \hat{\mathbf{p}} \tag{14}$$

and

$$\overline{\overline{\mathbf{G}}}_m^{\,b} \cdot \hat{\mathbf{p}} = i\frac{e^{-ikr}}{4\pi r}\left(\mathbf{k}_t \times \overline{\overline{\mathbf{T}}}_e e^{ik\hat{\mathbf{r}}\cdot\mathbf{r}_g{}'} e^{ikz_b{}'\sqrt{n^2-\sin^2\theta}}\right) \cdot \hat{\mathbf{p}} \tag{15}$$

where $\mathbf{k} \times \overline{\overline{\mathbf{I}}}$ etc. are the *anterior* vector products [11] and where

$$\begin{aligned} \mathbf{k} &= k\hat{\mathbf{r}} = k(\sin\theta\hat{\mathbf{x}} + \cos\theta\hat{\mathbf{z}}) \\ \mathbf{k}_r &= k(\sin\theta\hat{\mathbf{x}} - \cos\theta\hat{\mathbf{z}}) \\ \mathbf{k}_t &= k(\sin\theta\hat{\mathbf{x}} + \sqrt{n^2-\sin^2\theta}\hat{\mathbf{z}}) \end{aligned} \tag{16}$$

are the propagation vectors of the direct, reflected and refracted waves. Although the derivation above assumes that $\hat{\mathbf{r}}$ lies in the $X-Z$ -plane, the Green's functions can be easily generalized for arbitrary scattering angles by applying a proper rotational matrix.

$\overline{\overline{\mathbf{R}}}_e$ and $\overline{\overline{\mathbf{T}}}_e$ will be frequency dependent if losses are present in the ground, i.e. $\sigma \neq 0$ in (11). In this case, it is not straightforward to transform these Green's functions (6), (12), (14) and (15), into the time-domain. Therefore, the Green's functions are divided into separated parts; one part which can be easily transformed into the time-domain and one part that is maintained in the frequency domain.

For simplicity, we exemplify the derivation using only the first integral in (1), corresponding to the magnetic far-zone vector potential $\mathbf{A}$. In the far-zone, the polarization vector $\hat{\mathbf{p}}$ is transverse to $\hat{\mathbf{r}}$ and can therefore be expressed in the unit vectors $\hat{\theta}$ or $\hat{\varphi}$. Applying the scalar product $\hat{\mathbf{p}} \cdot \mathbf{A}$, the magnetic vector potential for a certain polarization can be determined, denoted A_p where $p = \theta$ or $p = \varphi$. Using (1) and (6) the contribution to the frequency domain vector potential from sources above the surface can be written as

$$A_p^a(\omega) = \frac{\mu_0 e^{-ikr}}{4\pi r} \left(A_p^0 + \mathbf{A}_R \cdot \mathbf{R}_{ep} \right) \tag{17}$$

where

$$A_p^0(\omega) = \iint_{S_a} (\hat{\mathbf{n}} \times \mathbf{H}_s(\omega, \mathbf{r}')) \cdot \hat{\mathbf{p}} e^{ik\hat{\mathbf{r}} \cdot \mathbf{r}'} dS', \tag{18}$$

$$\mathbf{A}_R(\omega) = \iint_{S_a} (\hat{\mathbf{n}} \times \mathbf{H}_s(\omega, \mathbf{r}')) e^{ik\hat{\mathbf{r}} \cdot \mathbf{r}_r{}'} dS' \tag{19}$$

and

$$\mathbf{R}_{ep} = \overline{\overline{\mathbf{R}}}_e \cdot \hat{\mathbf{p}}. \tag{20}$$

The surface integral is performed on the part of S that is above the ground, denoted S_a in Fig. 1.

By dividing the vector potential into these parts we can avoid a complicated convolution integral. Both A_p^0 and $\mathbf{A}_R$ can be easily transformed into the time domain:

$$A_p^0(t) = \iint_{S_a} (\hat{\mathbf{n}} \times \mathbf{H}_s(t + \frac{\hat{\mathbf{r}} \cdot \mathbf{r}'}{c})) \cdot \hat{\mathbf{p}} dS' \tag{21}$$

and

$$\mathbf{A}_R(t) = \iint_{S_a} (\hat{\mathbf{n}} \times \mathbf{H}_s(t + \frac{\hat{\mathbf{r}} \cdot \mathbf{r}_r{}'}{c})) dS' \tag{22}$$

Note that the three Cartesian components of (22) depend on different H-field components, dependent on which side of S_a the integration is performed. The surface S_a is aligned to the electric grid in FDTD while the corresponding integration of the electric vector potential will be performed on a surface aligned to the magnetic grid adjacent to S_a, according to [10].

The time-domain parts of the vector potential are calculated during the FDTD-run which corresponds to an ordinary time-domain near- to far-zone transformation in FDTD [8], [10]. After the FDTD-run these parts are transformed into the frequency domain and the frequency domain vector potential is calculated simply by using (17). The procedure for obtaining the electric vector potential $\mathbf{F}$ is analogous. For source points above the surface the procedure is equivalent to a traditional free-space time domain transformation for FDTD, except that this procedure also requires extra storage for the vector time-domain array $\mathbf{A}_R$ (and $\mathbf{F}_R$).

For sources below the ground the situation is slightly different and requires more storage of data during the FDTD-run. Since the second exponential part in (12) includes both the integration coordinate z_b' and a complex frequency dependence (if losses are present), an array of temporary stored vector potentials must be used; one for each layer, l, below the ground corresponding to different values of z_b', see Fig. 2. The integration of the vector potentials are performed on the part of S that is extended below the ground, denoted S_b. For the four vertical surfaces of S_b below the ground-level, the temporary time-domain vector potentials are integrated along a closed path $C_b(l)$ at each $z_b'(l)$. One array every half Δz is necessary due to the different spatial shift of the field components in FDTD. The bottom surface is integrated as a whole since this surface is positioned at a constant z_b'-level. The magnetic vector potential from sources below the ground level can then be written as

$$A_p^b(\omega) = \frac{\mu_0 e^{-ikr}}{4\pi r} \mathbf{A}_{T\,tot}(\omega) \cdot \mathbf{T}_{ep} \tag{23}$$

where

$$\mathbf{T}_{ep} = \overline{\overline{\mathbf{T}}}_{\mathbf{e}} \cdot \hat{\mathbf{p}} \tag{24}$$

and

$$\mathbf{A}_{T\,tot}(\omega) = \sum_l \mathbf{A}_T(\omega, l) e^{ikz_b{}'(l)\sqrt{n^2 - \sin^2\theta}}. \tag{25}$$

The summation over l in (25) symbolize the l-indices from the surface level and below to the bottom part of S, and corresponds to the z'-part of the surface integration. On the four vertical sides of S_b the $\mathbf{A}_T$ vectors, one for each $z_b{}'$, are written as

$$\mathbf{A}_T(\omega, l) = \Delta z \oint_{C_b(l)} \hat{\mathbf{n}} \times \mathbf{H}_s(\omega, \mathbf{r}') e^{ik\hat{\mathbf{r}} \cdot \mathbf{r}_g{}'} |_{z' = z_b{}'(l)} ds' \tag{26}$$

where C_b is the closed contour around S_b at constant z'. At the bottom surface of S corresponding to $l = l_{min}$, $\mathbf{A}_T$ is calculated using a surface integral

$$\mathbf{A}_T(\omega, l_{min}) = \iint_{S_{b_{min}}} \hat{\mathbf{n}} \times \mathbf{H}_s(\omega, \mathbf{r}') |_{z' = z_b{}'(l_{min})} e^{ik\hat{\mathbf{r}} \cdot \mathbf{r}_g{}'} dS'. \tag{27}$$

Each $\mathbf{A}_T$ can be transformed into the time-domain analogously to (21) and (22). The temporary time-domain vector potential arrays then become

$$\mathbf{A}_T(t,l) = \Delta z \oint_{C_b(l)} \hat{\mathbf{n}} \times \mathbf{H}_s(t + \frac{\hat{\mathbf{r}} \cdot \mathbf{r}_g{}'}{c}, \mathbf{r}')ds' \qquad (28)$$

and

$$\mathbf{A}_T(t,l_{min}) = \iint_{S_{b_{min}}} \hat{\mathbf{n}} \times \mathbf{H}_s(t + \frac{\hat{\mathbf{r}} \cdot \mathbf{r}_g{}'}{c}, \mathbf{r}')dS'. \qquad (29)$$

Note that these time-domain arrays are calculated using a retarded time to the ground surface only. The time delay corresponding to propagation vertically in the ground will be added in the frequency domain after the FDTD-run using (25). The procedure for the electric vector potential is of course analogous. Due to the discrete nature of FDTD, the integrals in the equations above are replaced by summation when implemented in a program code.

The procedure can now be summarized (exemplified with the magnetic vector potential $\mathbf{A}$ here): A small number of temporary vector potentials are integrated across the enclosing surface in the time domain during the FDTD-run. This corresponds to an ordinary time-domain transformation in free space except that a few extra arrays for storage of the far-zone data must be used. After the FDTD-run these time-domain arrays are transformed into the frequency domain (preferable with an FFT) and the total vector potential can be formed simply by summing up the different contributions.

$$\begin{aligned} A_p(\omega) =& A_p^a(\omega) + A_p^b(\omega) = \\ & \frac{\mu_0 e^{-ikr}}{4\pi r} \left(A_p^0(\omega) + \mathbf{A}_R(\omega) \cdot \mathbf{R}_{ep} \right. \\ & \left. + \mathbf{A}_{T\,tot}(\omega) \cdot \mathbf{T}_{ep}\right) \end{aligned} \qquad (30)$$

where $\mathbf{A}_{T\,tot}(\omega)$ is a summation over the l -indices in the ground material according to (25). The procedure for the electric vector potential $\mathbf{F}$ is treated analogously and the final electric far-zone field can be calculated by

$$\begin{aligned} E_\theta &= -i\omega A_\theta - i\omega\eta F_\varphi \\ E_\varphi &= -i\omega A_\varphi + i\omega\eta F_\theta \end{aligned} \qquad (31)$$

where η is the free space wave impedance. These expressions correspond to (1) for the two different polarizations of $\hat{\mathbf{p}}$.

If desired the far-zone electric fields can then be transformed back to the time domain by an inverse FFT. A small remark is in place here; if the near- to far-zone transformation surface extends far below ground level, thereby including a large number of FDTD-layers, the number of temporary vector potential arrays might be large and memory consuming.

3 Results

In order to check the accuracy and time savings of the transformation a simple scattering object was chosen as a test case. A 0.6m ×0.6m dihedral was placed 0.285 m above the ground, which has a conductivity of $\sigma = 0.01$ S/m and a relative permittivitty of $\epsilon_r = 10$, see Fig. 3. This type of scattering object is of interest in VHF/UHF synthetic aperture radar imaging, discussed in [3]. The cell size was 0.03 m, which implies that the size of the dihedral is 20×20 cells. In FDTD, the reflection of plane waves at the air-ground interface occurs a half cell size above the top layer of horizontal electric field components in the ground. This means that the bottom plate of the dihedral defined in the electric FDTD-grid is positioned 9.5 cells above the ground (which is equal to 0.285 m)

Let us assume that we were interested in the backscattered far-zone field between 20 MHz and 700 MHz. The cell size was 0.03 m cubed which implies 14 cells per wavelength in free space at 700 MHz and only 4.5 cells per wavelength in the ground material. The size of the computational volume was $60 \times 60 \times 60$ cells and the outer boundary condition was an additional 6-layer PML (Perfectly Match Layer) [12]. The PML in the ground was treated in a similar way as described in [13].

Both a frequency and a time-domain transform was applied using this object. The angles of incidence are indicated in Fig. 3 and the incident field was applied using a Huygens' surface [14] 15 cells from the PML boundary.

Applying the time domain near- to far-zone transformation to this problem, the frequency resolution will be determined by the number of time-steps of the simulation since we will transform the time domain result into the frequency domain using a Fast Fourier Transform (FFT).

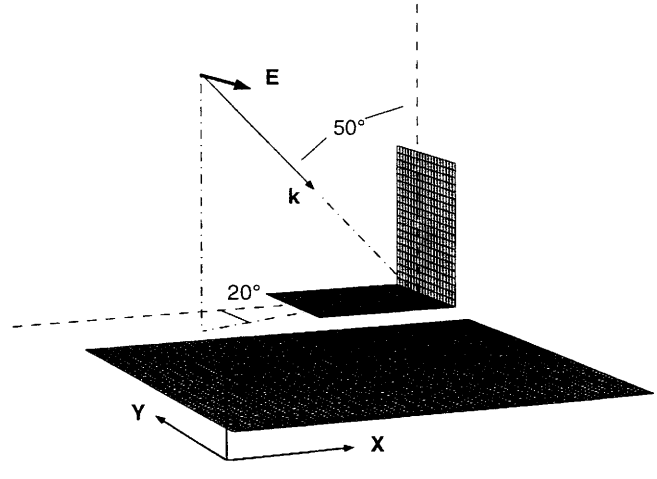

Figure 3: *Dihedral model both for FDTD and for MoM.*

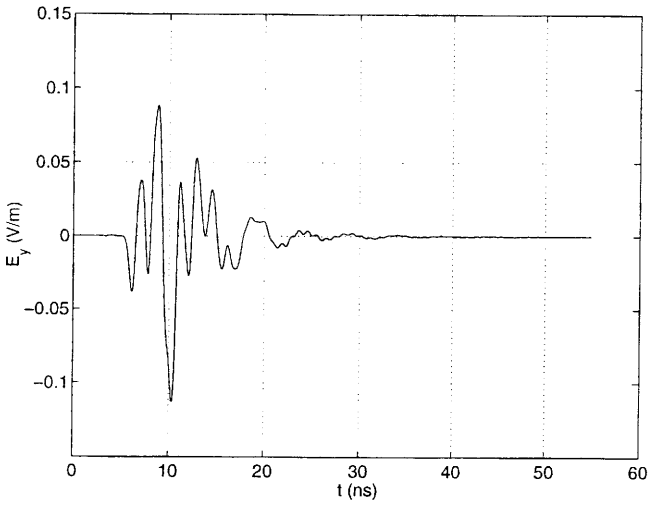

Figure 4: *Example of time-domain electric field in front of the dihedral when illuminated by a plane wave pulse with* $E_{inc} = \tau\sqrt{2e}\exp(-\tau^2)$ *V/m, where* $\tau = 4/(\beta\Delta t)(t - 1.5\beta\Delta t)$ *with* $\beta = 35$ *and* $\Delta t = 54.9$ *ps. The scattered field component* $E_y(15, 13, 30)$ *is shown.*

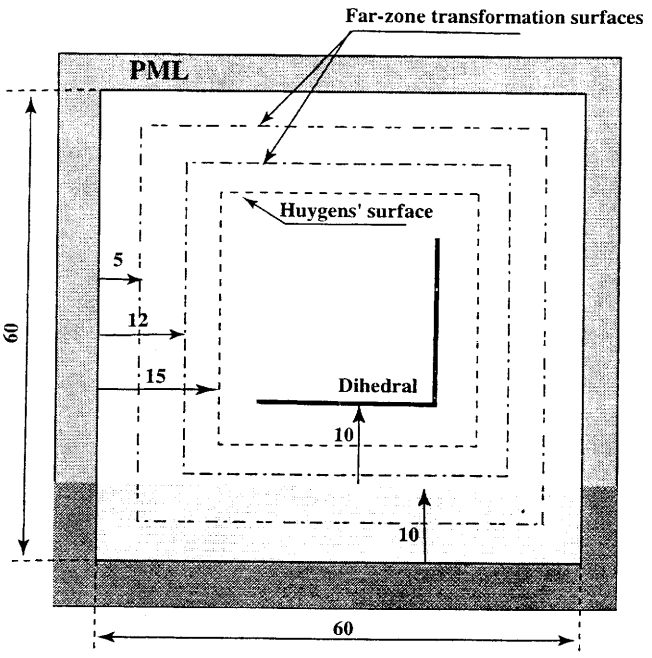

Figure 5: *X-Z slice of the computational volume at* $y = 30\Delta y$. *The different surfaces involved in the simulation are indicated in the figure. The distances are measured in number of FDTD-cells.*

For the frequency domain near- to far-zone transformation there is a free choice of frequency resolution. The question is how many frequency points within the frequency band of interest we should choose for the frequency domain transformation. Generally, there is no simple answer to this question, since object size, delays, resonances etc. can affect the response of the scattered fields. The crudest way is to make a test run in order to see how many time-steps are necessary for the scattering signal to decay. As a rule of thumb, the frequency interval should at least be

$$\Delta f \approx \frac{1}{T} \tag{32}$$

where T is the time it takes for the pulse response to decay when the object is illuminated by a plane wave pulse. As an example, the time response of the scattered field of the dihedral when illuminated by a Gaussian derivative pulse can be seen in Fig. 4. The figure shows the scattered horizontal electric field (E_y) obliquely in front of the dihedral (parallel to both dihedral plates). The calculation ran for 1000 time-steps and estimating the pulse response in Fig. 4 to be 50 ns, including a reasonable margin, gives $\Delta f = 20$ MHz. This means that we should choose at least 35 frequency points between 20 MHz and 700 MHz for the frequency domain transformation.

Several simulations were performed using the two different near- to far-zone transformation methods. Also, the surface on which the equivalent surface currents were extracted was also altered between two positions; one very close to the object, 12 cells from the PML boundary and one further away from the object, 5 cells from the PML boundary. The latter case implies that a larger number of fields below the ground had to be included in the transformation procedure. The area ratio between the transformation surfaces in the two cases is 1.93. The positioning of the different surfaces relative to the dihedral and the ground can be seen in Fig. 5.

Scattering results were also calculated using the Method of Moment code NEC-3. The mono-static radar cross section (RCS) of the dihedral for horizontal polarization can be seen in Fig. 6 and the corresponding phase of the far-zone field can be seen in Fig. 7. As seen in the figures, the correspondence is excellent. The phase reference point is in the middle of the computational volume.

The CPU time for the different FDTD-simulations are plotted in Fig. 8. The simulations using the frequency domain transformation were performed with three different numbers of frequency points between 20 MHz and 700 MHz in order to check the time dependence of this transform. The number of frequency points for the time domain transformation is dependent on the number of time-steps used in the FFT which was 2048 in this case (zeros padded). The vertical dash-dotted line in Fig. 8 indicates the lowest limit of desired frequency points according to (32), which is 35 in this case.

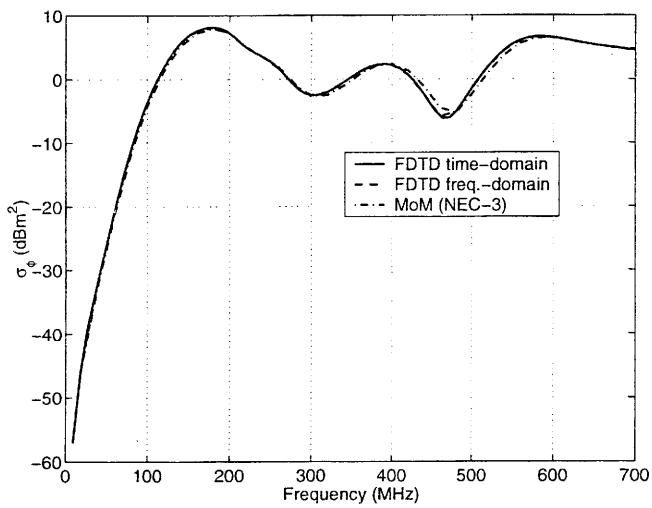

Figure 6: *Magnitude of RCS for dihedral using FDTD and for MoM. Both the frequency domain and the time-domain transformation results are shown in the plot.*

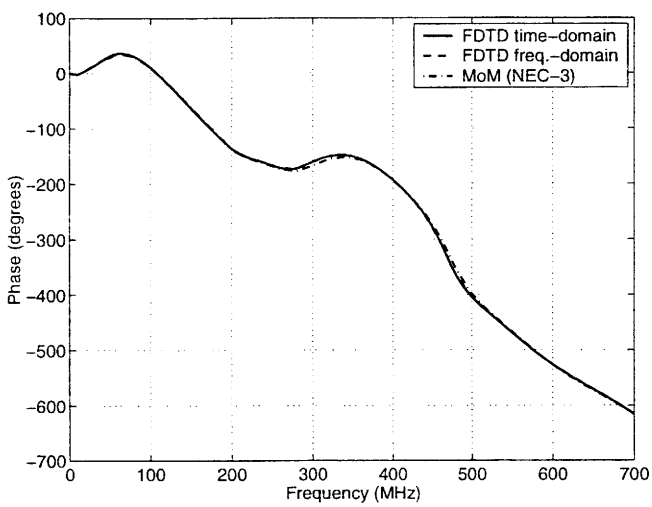

Figure 7: *Phase of far-field vector for dihedral using FDTD and for MoM. Both the frequency domain and the time-domain transformation results are shown in the plot. The phase reference point is in the middle of the computational volume, 10 cells above the dihedral bottom plate.*

In addition, a reference simulation was made without any near- to far-zone transformation. This time reference level is shown as a dotted line in Fig. 8. Note that the dashed lines for the different frequency domain transformations would cross the CPU-time axis at the time-level of the reference simulation if extrapolated to 0 frequency points.

As seen from the figure, the time-domain transformation is at least twice as fast as the frequency domain transformation if more than 35 frequency points are desired. This is due to the fact that the currents are transformed into the frequency domain using a DFT, which may become very time consuming. The additional CPU-time needed for the time domain transformation is very small compared to the CPU-time of the reference simulation. The near- to far-zone transformation is also sensitive to the size of the enclosed surface S on which the equivalent surface currents are calculated. The difference between the two transformation types would hence become even greater for larger sizes of computational volumes. The ratio between the slope of the two different frequency domain transformation curves corresponds well to the area ratio of 1.93 mentioned above.

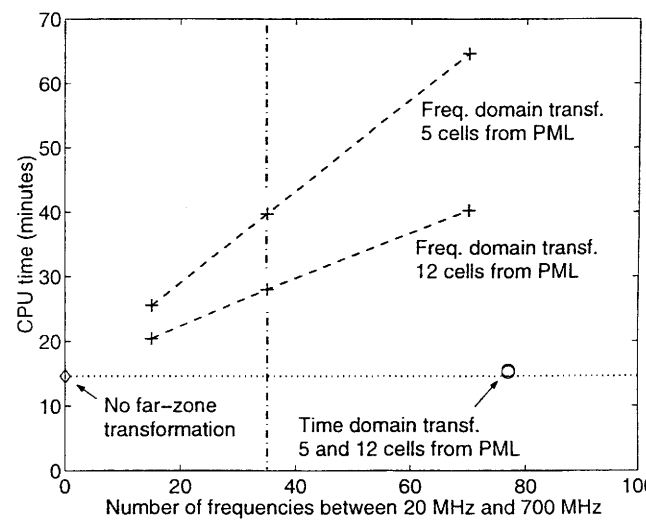

Figure 8: *CPU-time in minutes for the FDTD-simulations using frequency domain and time domain transformations. Two different sizes of the transformation volume have been used.*

4 Conclusions

A time domain version of the near- to far-zone transformation above a lossy dielectric half-space in FDTD has been developed. The far-zone Green's function has been divided into different parts of which some are treated

in a similar way as a traditional time-domain transformation in free space. After the FDTD-simulation, these parts are transformed into the frequency domain and the reflected and refracted parts are multiplied by the corresponding Fresnel coefficients. Finally, the different parts are added together to form the scattered field in the frequency domain. Significant time savings can be achieved if a large number of frequency points are desired. The time savings depend on the size of the transformation surface enclosing the object and the number of desired frequency points. Comparisons with a frequency domain transformation using a DFT, applied to a dihedral above ground, showed that the time-domain transformation was nearly a factor of two faster than the frequency domain transformation. The difference would probably be much greater if a larger problem size was considered, since the additional CPU-time for the time domain transformation is very small compared to CPU-time of the basic FDTD-algorithm, whereas the additional CPU-time for the frequency transformation increases dramatically with increasing area enclosing the scattering object.

References

[1] K. Demarest, Z. Huang, and R. Plumb, "An FDTD near- to far-zone transformation for scatterers buried in stratified grounds," *IEEE Trans. Antennas Propagat.*, vol. 44, no. 8, pp. 1150–1157, 1996.

[2] T. Dogaru and L. Carin, "Time-domain sensing of targets buried under a rough air-ground interface," *IEEE Trans. Antennas Propagat.*, vol. 46, no. 3, pp. 360–372, 1998.

[3] T. Martin and L. Ulander, "Far-zone transformation in FDTD for VHF-band SAR-image simulations," in *ACES 98.*, Monterey, CA, March, 16–20 1998, vol. 1, pp. 79–86.

[4] F.L. Teixeira, W.C. Chew, M. Straka, M.L Oristaglio, and T. Wang, "Finite-difference time-domain simulation of ground penetrating radar on dispersive, inhomogenous, and conductive soils," *IEEE Trans. Geosci. Remote Sensing.*, vol. 36, no. 6, pp. 1928–1937, Nov. 1998.

[5] N. Geng, M.A. Ressler, and L. Carin, "Wide-band VHF scattering from a trihedral reflector situated above a lossy dispersive halfspace," *IEEE Trans. Geosci. Remote Sensing.*, vol. 37, no. 5, pp. 2609–2617, Sept. 1999.

[6] H. Israelsson, L.M.H. Ulander, T. Martin, and J.I.H. Askne, "A coherent scattering model to determine forest backscattering in the VHF-band," *IEEE Trans. Geosci. Remote Sensing.*, vol. 38, no. 1, pp. 238–248, Jan. 2000.

[7] R. J. Luebbers, K. S. Kunz, M. Schneider, and F. Hunsberger, "A finite-difference time-domain near zone to far zone transformation," *IEEE Trans. Antennas Propagat.*, vol. 39, no. 4, pp. 429–433, 1991.

[8] T. Martin and L. Pettersson, "Dispersion compensation for Huygens' sources and far zone transformation in FDTD," *IEEE Trans. Antennas Propagat.*, vol. 48, no. 4, pp. 494–501, Apr. 2000.

[9] J. D. Jackson, *Classical Electrodynamics*, Wiley, New York, third edition, 1998.

[10] T. Martin, "An improved near- to far-zone transformation for the finite-difference time-domain method," *IEEE Trans. Antennas Propagat.*, vol. 46, no. 9, pp. 1263–1271, Sept. 1998.

[11] C.-T. Tai, *"Dyadic Green Functions in Electromagnetic Theory"*, IEEE press, New York, 2:nd edition, 1993.

[12] J.-P. Berenger, "A perfectly matched layer for the absorption of electromagnetic waves," *J. Comput. Phys.*, vol. 114, no. 1, pp. 185–200, 1994.

[13] J. Fang and Z. Wu, "Generalized perfectly matched layer for the absorption of propagating and evanescent waves in lossless and lossy media," *IEEE Trans. Microwave Theory Tech.*, vol. 44, no. 12, pp. 2216–2222, Dec. 1996.

[14] D. E. Merewether, R. Fisher, and F. W. Smith, "On implementing a numeric Huygen's source scheme in a finite difference program to illuminate scattering bodies," *IEEE Trans. Nucl. Sci.*, vol. 27, no. 6, pp. 1829–1833, 1980.